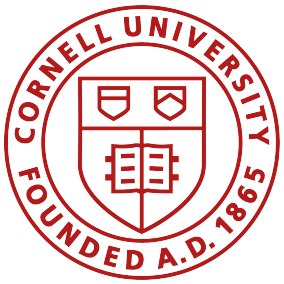

Design and Evaluation of a Water-Braking Mechanism for an Interfacial-Flight Insect-Scale Robot

Final Design Report

Lucca Correia

Cornell University
School of Mechanical and Aerospace Engineering
Helbling Research Lab

January 27, 2026

Contents

Abstract

This report presents the design and testing of a drag-based water brake for the Gammabot, an insect-scale flapping-wing robot that skims along the water surface. The brake is intended to slow the robot from its measured top speed of 0.7 m/s to within 5% of that value over a stopping distance of 6 cm, while preserving interfacial operation and avoiding any breaking of the water surface. The Gammabot wings are unable to provide a reverse thrust force, thus there is currently no active control over the robot's ability to stop and maintain position. This braking capability does not only enable better obstacle avoidance but is part of a broader effort to allow these robots to communicate via wing-generated ripples while positioned side by side on the water. The brake is crucial for allowing a robot to decelerate quickly enough to stop near a neighbor and maintain its position throughout communication. The physical prototype consists of a lightweight carbon-fiber flat-plate brake designed to leverage form drag and maximize strength to weight ratio. It integrates with the current chassis via a pin-and-slot mounting bracket for repeatable, modular adjustment of immersion depth while minimizing added mass and preserving chassis compatibility. At the modeling level, the braking behavior is characterized by a lumped drag parameter K that governs how quickly velocity decays with distance, and a target value is derived and compared against experimentally determined values at different plate immersion depths. Quantative results showed that the brake reduces stopping distance by an average of one third that of the no-brake baseline, and the velocity–distance profiles reflect a substantial, repeatable increase in deceleration. The weak separation between the braked depths is likely due to the short runway and lower-than-target initial speeds, which reduce sensitivity to depth-dependent changes in K. Nonetheless, the clear performance gap between braked and unbraked runs validates the effectiveness of the water brake and motivates a next-generation experiment with an actuated brake and more precisely controlled thrust.

1 Introduction

Many semi-aquatic insects exploit the air-water interface as a unique locomotion environment where surface tension allows species such as water striders, fishing spiders, stoneflies, and waterlily beetles to rest on the surface with minimal energetic cost while generating thrust through sculling or flapping motions. Building on these biological strategies, prior work in the Helbling Lab introduced the Gammabot, an insect-scale flapping-wing robot that operates on the air-water interface [2]. The vehicle uses passive skis that allow the robot to rest on the interface via surface tension, while independently-driven wings generate thrust

and turning moments parallel to the surface, enabling high-speed interfacial flight and agile maneuvers. The second-generation Gammabot has a mass of 0.898 g and is capable of supporting an additional load of $\approx$ 1.5 g. The braking mechanism presented is part of this second-generation Gammabot extended toward controlled stopping and close-proximity behaviors needed for future multi-robot communication experiments.

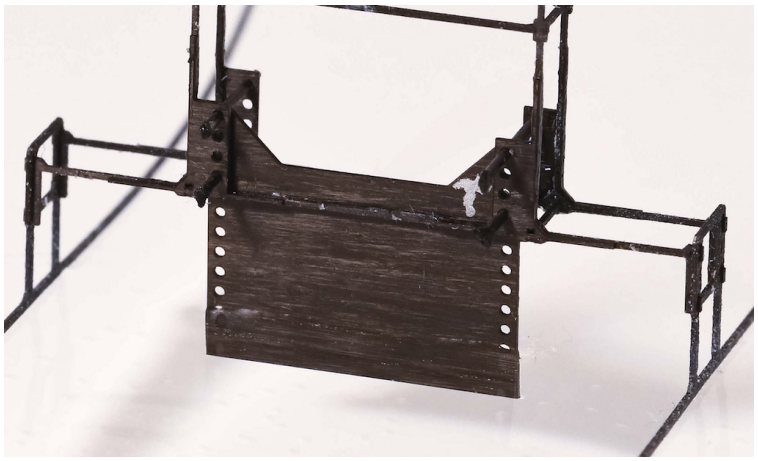

Figure 1: Brake Plate Close Up

Several brake concepts were explored and evaluated against early braking-force requirements as well as manufacturing, integration, testing, and modeling complexity. The selected design leverages water's high density through form drag on a thin plate while remaining more simple to fabricate and applicable to existing modeling from literature. Fig. 1 shows a stripped down version of the final prototype, highlighting the carbon-fiber–resin laminate sheet that spans the leg spacing of the Gammabot and the four swappable carbon-fiber rods that allow for a quick, repeatable way to vary immersion depth between trials. For current testing, this passive depth-adjustable brake is mounted on a outfitted Gammabot chassis which interfaces with a magnetic straight-line rail and tested at multiple depths. Note that the brake has not yet been actuated; results here are intended to provide confidence in the general braking design as well as experimentally derive a lumped parameter specific to the Gammabot to relate velocity and stopping distance that will inform the next-generation actuated system.

Starting from the quadratic drag law $F_D = \frac{1}{2}\rho C_D A v^2$ and Newton's second law, we derive an exponential velocity–distance relation $v(x) = v_0 e^{-Kx}$, where the lumped drag constant $K = \frac{1}{2}(\rho C_D A)/m$ governs how quickly velocity decays with distance. Written in terms of the performance metrics: $K_{\text{target}} = \frac{1}{x_{\text{stop}}} \ln\left(\frac{v_0}{v_f}\right)$, this model can be used to define a target drag constant K_{target} and corresponding first-order area estimate that would achieve the desired stopping distance, which we then compare against experimentally calibrated values of the

effective drag constant K_{exp} as a function of brake immersion depth.

Using repeated braking trials, we fit an exponential decay model to the measured motion to extract K_{exp} at different depths and verify that it is largely insensitive to the range of initial velocities achievable in the tank. Additionally, the clear difference between braked and no-brake cases validates the brake's effectiveness. However, the lack of variation between K values among braked-depths motivates a second experiment with an actuated brake and more precisely controlled thrust aimed to provide further resolution between these depth trials. This will provide a more reliable relationship between K_{exp} and K_{target}, and in turn, a analytical relationship between stopping-distance requirement and brake depth.

2 Alternative Design Concepts

2.1 Alternative Designs

- **Air Brake** – Conceptually similar to the water brake, however this design deploys a flat plate into the air stream of the robot. The air brake was considered as an alternative to the water brake plate in case preliminary calculations showed that aerodynamic form drag alone (without exploiting water's higher density) could meet the performance requirements.

- **Skin Friction Mat** – Design entails deploying a plate parallel to the water's surface and leveraging skin friction via contact with the water's surface rather than form drag in the water.

- **Rod with Varied Front and Rear Contact Angles** – This concept uses a slender rod that spans perpendicular to the direction of motion and lightly contacts the water surface. By applying a larger hydrophilic coating on the downstream face than on the upstream face, the rod generates asymmetric contact angles with the free surface, denoted α_1 (front) and α_2 (rear). Fig. 2 shows the variables in a diagram from the previous Gammabot model. The meniscus at the rear of the rod extends from azimuthal angles ψ_1 to ψ_2 and the contact angle $\alpha(\psi)$ is assumed to vary smoothly between α_1 and α_2. Following the surface tension formulation used in [2], the streamwise component of the surface–tension force is

$$F_{s,x} = \int_{\psi_1}^{\psi_2} 2\gamma \cos\big(\alpha(\psi)\big)\, dR_L \sin\psi, \tag{1}$$

where γ is the surface–tension coefficient and R_L is the radial distance along the rod.

When $\alpha_1 \neq \alpha_2$, this integral yields a nonzero net surface–tension force directed opposite to the robot's motion, so the more hydrophilic downstream face is intentionally used to create a capillary "pull" that, together with viscous drag, enhances the braking force even at low forward velocities.

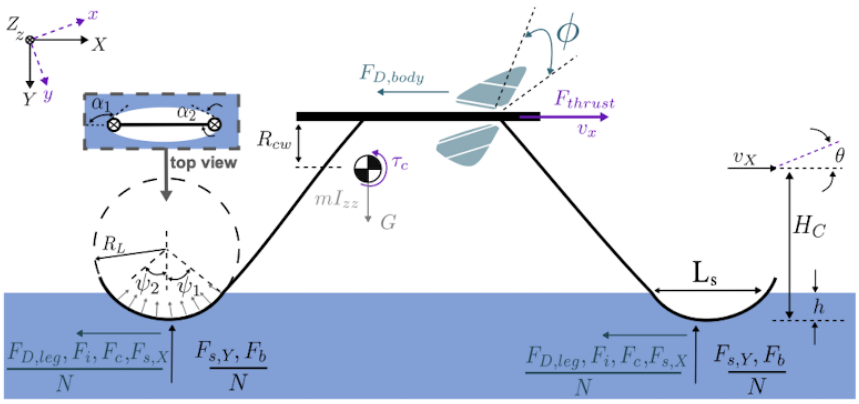

Figure 2: Rod Design Diagram [2]

- **Hydrophilic Comb** – This concept uses a lattice of thin plates oriented perpendicular to the direction of motion that lightly contact, but do not pierce, the water surface. The vertical faces of each plate that interact with the water column (and their corresponding opposite faces) are coated with a hydrophilic material to wick water upward with the forces outlined in [3]. In principle, the capillary-induced pressure gradient provides a drag force during motion and also a small surface–tension restoring force between the hydrophilic walls and the water. The motivation for introducing this surface–tension force is that it can act even when the robot's velocity is zero, whereas the drag force scales with V^2 and therefore vanishes as $V \to 0$.

- **Angled Skis** – The angled ski design involved angling the skis (bringing the tips closer together) to increase the effective area perpendicular to the direction of motion. The assumption was that this would increase area along which the Gammabot has to push the miniscus through the water with the same primary forces as in Eq.(1).

2.2 Final Design Justification

The design analysis began with an estimate of the force required to stop the robot moving at 0.7 m/s within 6cm, and each design was then evaluated on its ability to deliver that force while minimizing complexity, added mass, and modelling difficulty. For an object of mass

m, the mean acceleration needed to slow from v_0 to v_f over distance x_{stop} is

$$a = \frac{v_0^2 - v_f^2}{2x_{\text{stop}}} = \frac{(0.7 \text{ m/s})^2 - (0.05 \cdot 0.7 \text{ m/s})^2}{2\,(0.06 \text{ m})} = 4.07 \text{ m/s}^2. \tag{2}$$

The equivalent average braking force for the Gammabot mass $m = 0.000898$ kg would need to be approximately

$$F = ma = 3.65 \times 10^{-3} \text{ N}. \tag{3}$$

With this force esimation, we can use a simple drag model for a flat plate perpendicular to flow and immiediately roll out the airbrake which would require an unrealistically large area on the order of 6000m^2 calculated below

$$F_D = \tfrac{1}{2}\,\rho_{\text{air}} V^2 C_D A, \tag{4}$$

the required area for an air brake at $F \approx 3.65 \times 10^{-3}\,\text{N}$, $V = 0.7$ m/s, $\rho_{\text{air}} \approx 1.2$ kg/m^3, and $C_D \approx 2$ per [4] is

$$A_{\text{air}} = \frac{2F}{\rho_{\text{air}} V^2 C_D} = \frac{2(3.65 \times 10^{-3} \text{ N})}{(1.2 \text{ kg/m}^3)\,(0.7 \text{ m/s})^2 \cdot 2} \approx 6.2 \times 10^{-3} \text{ m}^2 \approx 6200 \text{ mm}^2. \tag{5}$$

If the same design leveraged the water density (1000 times that of water), the corresponding is not on the scale that would be implementable on the Gammabot. I also met with MAE Prof. Brian Kirby who helped rule out the other designs that relied on surface tension. He adivsed that surface tension tends to be orders of magnitude weaker than form drag and also introduce added complexity which may not be necessary to begin with. From here I settled on my current design of a thin carbon fiber brake plate that will be tested perpendicular to the flow.

3 Analysis and Modeling

In this modelling section, the braking dynamics are modeled as an exponential decay in distance to capture all uncertain hydrodynamic effects in a single lumped drag constant K (e.g., effective C_D, wetted area, and immersion-depth effects that are not easily modeled or captured by hydrodynamic equations.) without requiring each term to be known for each specific operating condition. Expressing the braking requirement in terms of K makes it directly comparable to experiments, since it depends only on the velocity ratio v_f/v_0 and the stopping distance and is therefore relatively immune to small variations in initial speed. The derivation of K and its use in selecting a target brake area is outlined in this section.

3.1 Background

The hydrodynamic drag force acting on the robot is given (4) where ρ is the water density, C_D is the drag coefficient, A is the projected wetted area, and v is the velocity. Applying Newton's second law:

$$m\frac{dv}{dt} = -\tfrac{1}{2}\rho C_D A v^2. \tag{6}$$

Defining the drag constant

$$K = \frac{1}{2}\frac{\rho C_D A}{m}, \tag{7}$$

we obtain

$$\dot{v} = -Kv^2. \tag{8}$$

3.2 Analytical Relation Between Velocity and Distance

To rewrite the dynamics in terms of distance x, we use $\dot{x} = v$ and apply the chain rule,

$$\frac{dv}{dx} \;=\; \frac{dv/dt}{dx/dt} \;=\; \frac{\dot{v}}{\dot{x}} \tag{9}$$

Substituting $\dot{v} = -Kv^2$ and $\dot{x} = v$ gives

$$\frac{dv}{dx} \;=\; \frac{-Kv^2}{v} \;=\; -Kv \tag{10}$$

Integrating from the initial condition v_0 at $x = 0$ to $v(x)$ at position x:

$$\int_{v_0}^{v(x)} \frac{dv}{v} = -K\int_0^x dx, \tag{11}$$

$$\ln\left(\frac{v(x)}{v_0}\right) = -Kx, \tag{12}$$

$$v(x) = v_0 e^{-Kx} \tag{13}$$

3.3 Determining the Target Drag Constant K_{target}

$$K_{\text{target}} = \frac{1}{x_{\text{stop}}}\ln\left(\frac{v_0}{v_f}\right) \tag{14}$$

In this experiment, the Gammabot slows from $v_0 = 0.7\,\text{m/s}$ to $v_f = 0.05v_0 = 0.035\,\text{m/s}$

in $x_{\text{stop}} = 0.06\,\text{m}$:

$$\begin{aligned} K_{\text{target}} &= \frac{1}{0.06} \ln\left(\frac{0.7}{0.035}\right) \\ &= 49.93 \end{aligned}$$

This value represents the braking strength in an ideal world that the physical brake geometry would need to achieve to meet the proposed performance metrics.

3.4 Area Range Estimation

Before designing the brake, an upper bound area needs to be calculated. Two complementary methods were used to obtain a first-order estimate of the braking surface area required for the Gammabot to slow from $v_0 = 0.7\,\text{m/s}$ to within 5% of that speed ($v_f = 0.035\,\text{m/s}$) over a stopping distance of $x_{\text{stop}} = 0.06\,\text{m}$. Both approaches assume water at $\rho = 1000\,\text{kg/m}^3$ and a drag coefficient $C_D \approx 2.0$ [4] representative of a flat plate normal to the flow.

Method 1: Constant Drag Force Approximation

We already calculated a simple constant-force estimate for the average braking requirement in Eq (3). If we rearrange the drag equation

$$F = \tfrac{1}{2}\rho C_D A v^2$$

for area and substitute our earlier result of $F = 3.65 \times 10^{-3}$ N, representative velocity $v_{\text{mean}} = (v_0 + v_f)/2 = 0.368$ m/s, and other parameters, we obtain

$$A = \frac{2F}{\rho C_D v_{\text{mean}}^2} = 2.70 \times 10^{-5}\ \text{m}^2 = 27.0\ \text{mm}^2. \tag{15}$$

Note that Method 1 provides a rough, constant-drag-force and linear velocity estimate suggesting a wetted area on the order of $A \approx 27$ mm^2, and is used only as an order-of-magnitude check on Method 2. Method 2 is more accurate because it retains the full quadratic velocity dependence of drag and yields an exponential velocity–distance relation governed by the lumped parameter K, rather than approximating the braking force as constant (or implicitly assuming a linear change in velocity) through averaging.

Method 2: Target Drag Constant (K_{target}) Approach

A more analytical estimate uses the exponential velocity–distance model:

$$v(x) = v_0 e^{-Kx}.$$

Where we already rearranged to derermine K_{target} earlier as 49.93 m^{-1}.

From the drag constant definition Eq. (7),

$$K = \frac{1}{2}\frac{\rho C_D A}{m},$$

the corresponding target area for the robot mass of $m = 0.000898$ is

$$A_{\text{target}} = \frac{2K_{\text{target}} m}{\rho C_D} = 44.8 \text{ mm}^2. \tag{16}$$

Comparison

Both methods yield consistent results:

$$A \approx 25\text{–}45 \text{ mm}^2,$$

corresponding to an immersion depth between roughly 1.5–3 mm for the 15.1 mm-wide braking panel (constraint defined lower in the design section). Because drag effects decay with v^2 as the robot slows, treating the braking force as constant (based on some "average" speed) makes the force appear too strong late in the stop, so Method 1 predicts *too small an area* compared to Method 2. The testing brake will have a maximum depth of 5 mm to account for effects not accounted for in the ideal models.

4 Prototype Design and Implementation

This section explains each brake component's design, fabrication, and assembly, with full experimental details presented in Section 6.1. At a high level, the experimental setup consists of a shallow tank of water (3.5 cm depth), a straight-line magnetic guide rail to constrain the robot to one-dimensional motion, and a fan used to provide a controlled impulse to the robot at the beginning of each trial.

4.1 Initial Design Considerations and CAD Model

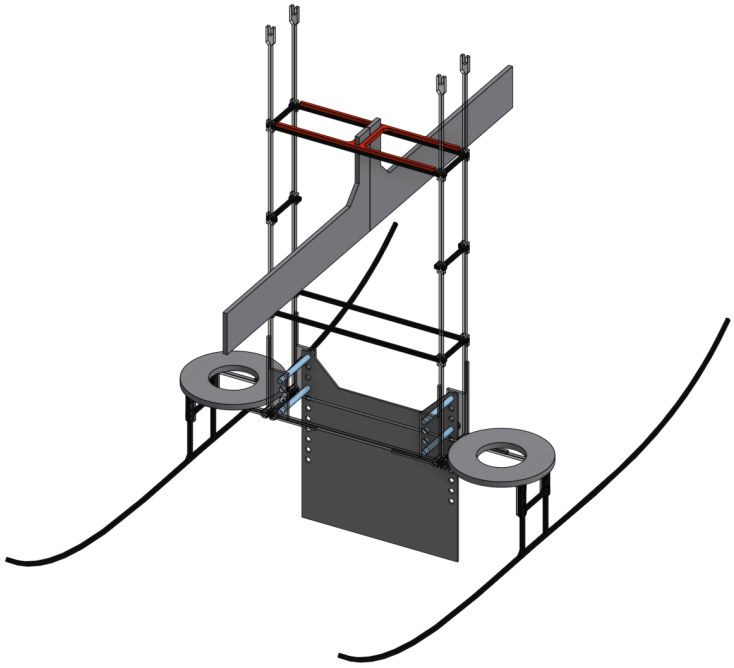

Figure 3: Full CAD assembly of the Gammabot braking system.

To test a range of brake depths, a modular setup was required that mounts to an existing Gammabot chassis to reduce fabrication complexity. The assembly also incorporates calibrated ballast to match the mass of a fully outfitted robot (electronics and wings) without exceeding the target mass or causing the skis to break surface tension (full CAD model shown in Fig. 3). All braking attachments were fabricated from existing carbon-fiber–resin laminate stock (255 µm thick plates with layer data from [5]) and carbon-fiber rods (0.5 mm diameter). These stock plates are manufactured in-house by pressing five carbon-fiber and resin layers together under high pressure, with the resin bonding the fiber plies into a single laminate. Senior lab members advised that, for the expected loading conditions, neither maximum bending stress nor interlaminar shear would be limiting, and that the lab's carbon-fiber laminate stock provides sufficient strength for this experiment; additionally, the brake plate was oriented to align with the fiber direction that maximizes bending stiffness and strength.

Tolerance Note

The rods have a factory tolerance of 0.4975 ± 0.0015 mm. Additionally, the lab's LPKF Protolaser U4 laser cutter has a laser beam width of 0.015 mm which means that the actual hole diameter on the top side could be up to ≈ 0.530 mm, and on the bottom side it would

be smaller (the cross-section is similar to an inverted trapezoid), so it is difficult to assign a precise value. This tolerance stack-up is addressed by fabricating a small laser-cut gauge with holes starting at 0.500 mm and increasing by 5 µm increments. We inserted the 0.5 mm rods into each hole until a proper interference fit was achieved; this occurred at the 0.515 mm diameter hole. This interference fit was crucial to ensuring that the plate would not slide along the rods and that the rods would not be able to slide free from the bracket slot holes mounted to the chassis.

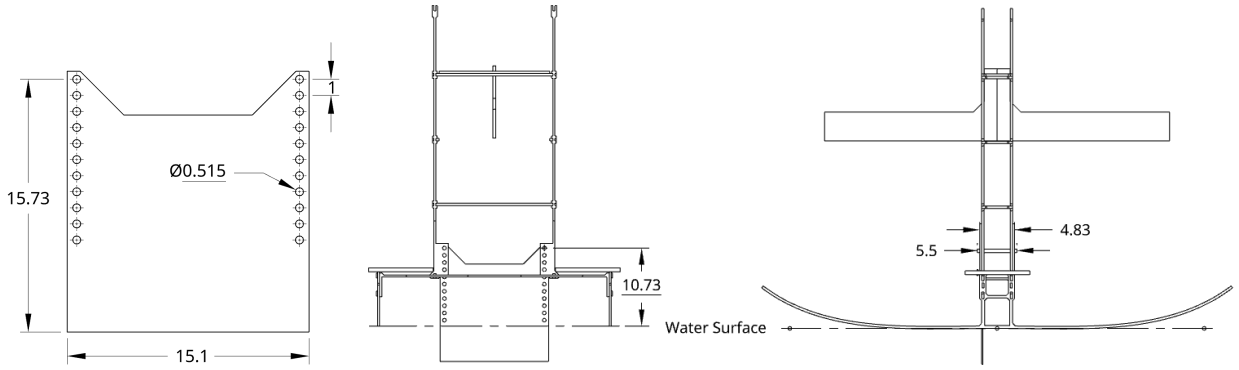

(a) Brake plate drawing (b) Full robot front and right

Figure 4: Key dimensions from model (all units in mm)

Pin Slot Brackets and Rods

Two sets of rods were installed on each side of the robot to support the brake plate, reducing bending and shear stresses on the pins and limiting lateral sliding. As shown in Fig. 4b, the rod length was set to 5.5 mm to extend beyond the 4.83 mm slot spacing; the additional length allowed the rod ends to be flattened to form heads that simplify handling during assembly and act as mechanical stops. The slot hole diameters were set to 0.515 mm as determined above, ensuring interference fit between holes and rods.

Brake Plate

The brake plate was designed to reduce weight and maximize mounting points to allow for many brake depths. The notch at the top reduces unessesary support material and the center-to-center 1 mm vertical gap between holes allows for a high resolution of brake depths while allowing for substantial support material between holes. The horizontal distance between holes is set to match the holes between mounted pin slot brackets. From Fig. 4b you can see that the height from the water's surface (disregarding any miniscus effects) and the top hole of the brake plate is 10.73 mm. Thus the height from the bottom of the brake plate to the

top hole is set to 10.73 mm + 5 mm = 15.73 mm in order to have a maximum testing depth of 5 mm. Note that testing data from the Gammabot shows that miniscus height tends to be 2 mm - 3 mm, thus the maximum testing brake depth could be as much as 8 mm.

Magnet Rail Interface

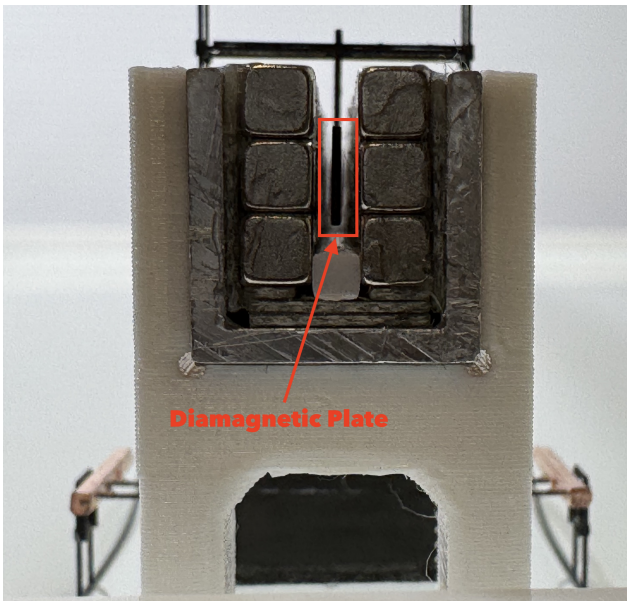

Figure 5: Diamagnetic Levitation in Magnetic Rail

A senior lab member previously developed a straight-line magnetic test rail that levitates diamagnetic plates; its use in this experiment is shown in Fig. 5. Because the blower thrust is not explicitly modeled, this rail is used to constrain the robot to one-dimensional motion and ensure that all thrust is translated into forward acceleration. The diamagnetic plate holder (shown in red in Fig. 3) mounts to the top level of the chassis and secures the custom-cut plate from above. The selected diamagnetic plate length has been demonstrated in prior experiments to provide sufficient lift for the robot mass supported on surface tension, while also generating a lateral restoring force that keeps the robot centered on the rail.

Added Weights

The two washers shown in Fig. 3 represent the added mass of the electronics and wings that would be mounted on the chassis; this additional weight affects the meniscus height as well as the robot's momentum and acceleration, so it must be replicated in testing. However, because stainless-steel washers would interact with the magnetic rail, two copper wires were instead fastened to the robot (see Fig. 11), each weighing 0.223 g, increasing the total mass

from 0.464 g to 0.91 g, which closely matches the mass of a fully equipped Gammabot.

4.2 Manufacturing

Laser Cutting

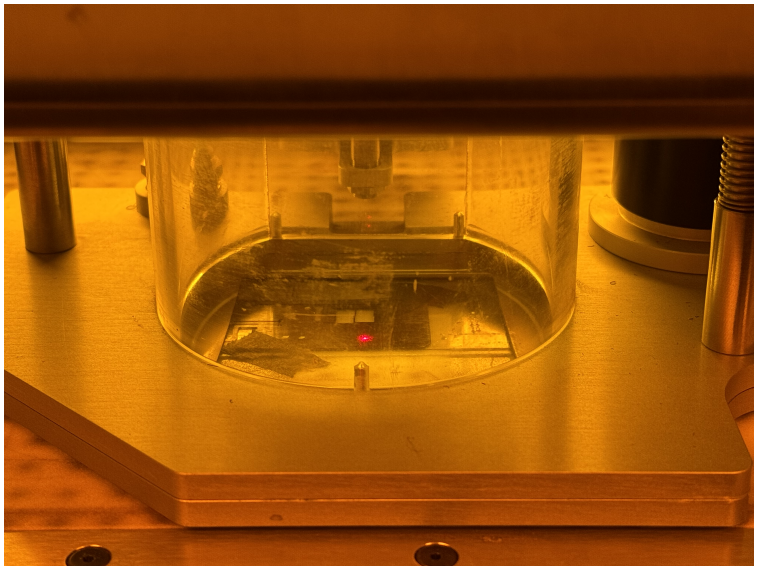

Figure 6: Laser Cutting Brake Plate

After finalizing the CAD model, the brake plate, pin slot brackets, and magnetic rail supports were laser cut in the lab's LPKF Protolaser U4 laser cutter. Senior lab members assisted in recommending laser settings (passes, intensity, speed) for my particular carbon-fiber–resin laminant stock informed by extensive tuning. Fig. 6 shows the carbon fiber plate mounted in place underneath the laser head.

Assembly

(a) Full Robot View (b) Microscope View

Figure 7: Second Level Removal for Magnetic Rail

After all parts were laser cut, they were assmbled under a microscope (6.3X magnification) with a work setup shown in Fig. 8. Before mounting the laser cut parts, we began by making a modification to an existing chassis: in Fig. 7a you can see the second level removal to provide clearance for the magnetic rail to pass through. Fig. 7b shows a close up of the removal of a carbon-fiber rod on the second level. One-hundred percent isopropanol was intermittently used to remove x-acto knife saw dust and external debris.

Next, the rod slot brackets Fig. 9c were mounted (entire process shown in Fig. 9). The loctite superbonder 495 ADH glue used does not adhere well to the hydrophobic coating thus it was scraped off first. Then a needle-tip-amount of glue was applied and the brackets were mounted and left to dry for 20 minutes. At this scale, the glue helps to pull the brackets into place and improve alignment with the through rods. A very similar glue-and-place procedure was followed to secure the diamagnetic support structure.

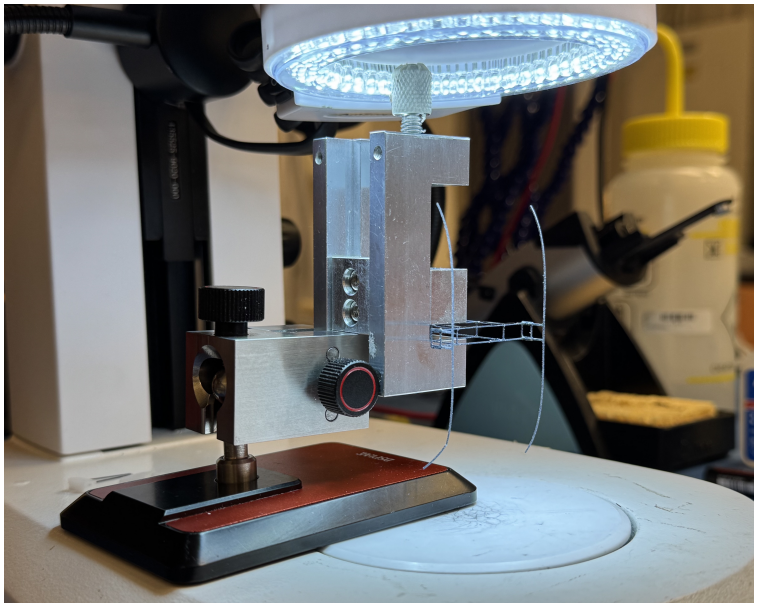

Figure 8: Fabrication Setup

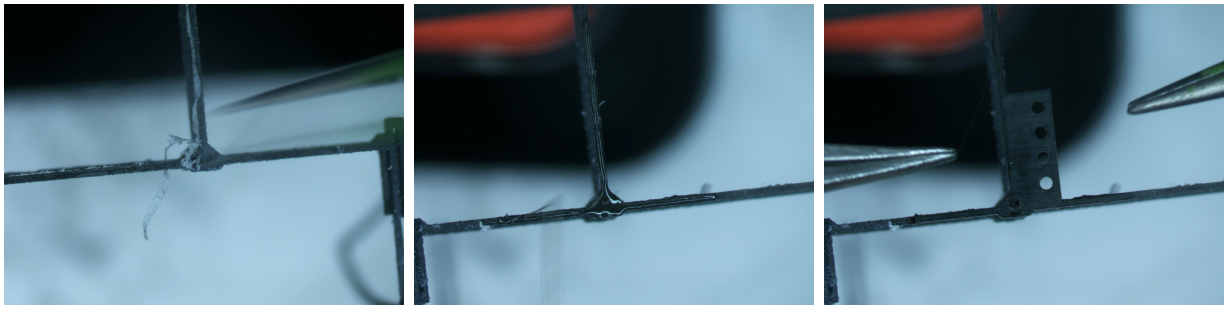

(a) Remove Coating (b) Apply Glue (c) Place Pin Slot Brackets

Figure 9: Sequence of brake engagement at the water surface.

4.3 Final Design

Fig. 10 and Fig. 11 show the final protptype used for the experiment.

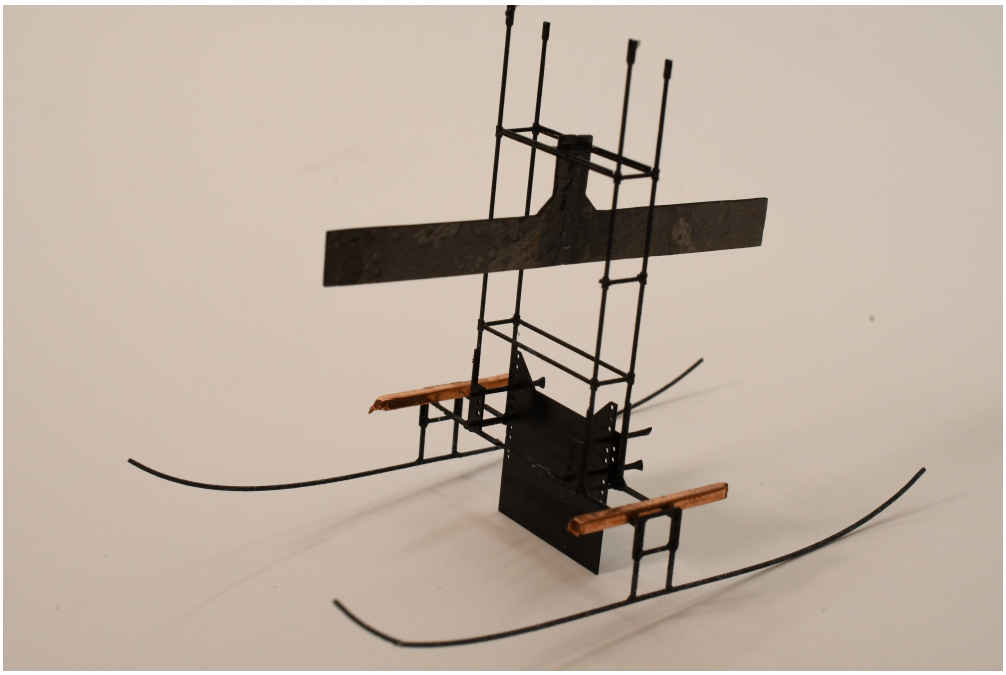

Figure 10: Final Design

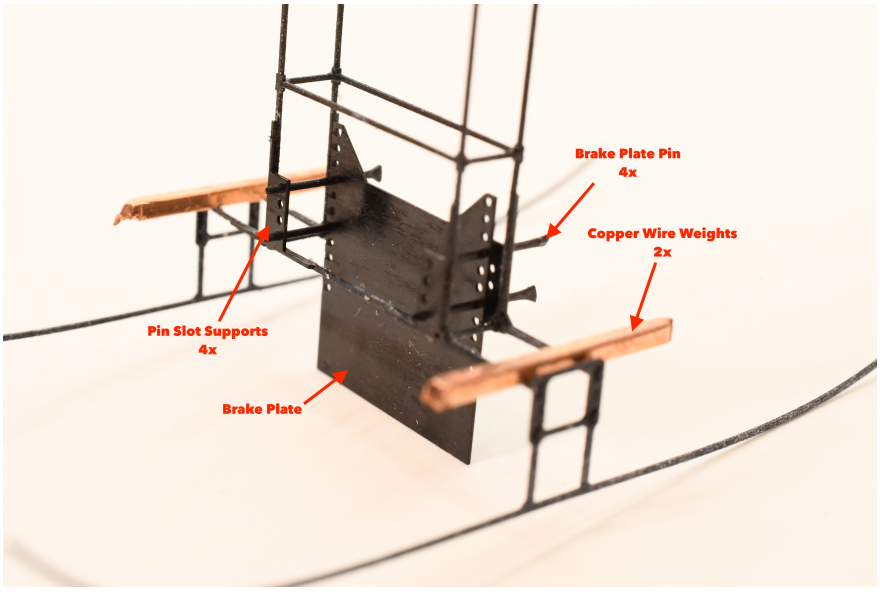

Figure 11: Bottom Half Part Identification

5 Experimental Methods

5.1 Setup

Fig. 12 shows the experimental setup used for all data collection. A 37 cm magnetic rail rests on two 3D printed supports which are fastened to the bottom of the tank via double-sided tape. The blower outlet was positioned 14.5 cm above the water surface and 30 cm upstream of the rail start, which produced a directed, repeatable impulse without generating excessive surface turbulence or forcing the robot to break surface tension. An air-shutter wall controlled the impulse duration: the robot was released from the right end of the tank, the shutter was opened to expose it to the blower, and then re-closed when the robot reached approximately mid-rail (a location marked to improve consistency across trials).

It is crucial that there is a consistent water level across the tank. If not, the magnetic rail (which is fastened to the tank and thus always level to it) will provide varied forces to the robot as it progresses along the rail. Water was added to the tank until the robot was supported by surface tension on the rail (shown in Fig. 13b). From there, the water level was tuned until every position along the magnetic rail showed a gap between the bottom of the diamagnetic plate and the magnetic rail (shown in Fig. 13); this ensured that the robot was not experiencing any rubbing friction during the entire trial. Across trials, each corner was measured at 3.5 cm depth and a buble level was used to ensure the tank remained level.

The lab high-speed camera was operated at 200 fps with a resolution of 832×800 pixels and a preset exposure time, which provided sufficient resolution to track the robot while keeping file sizes manageable.

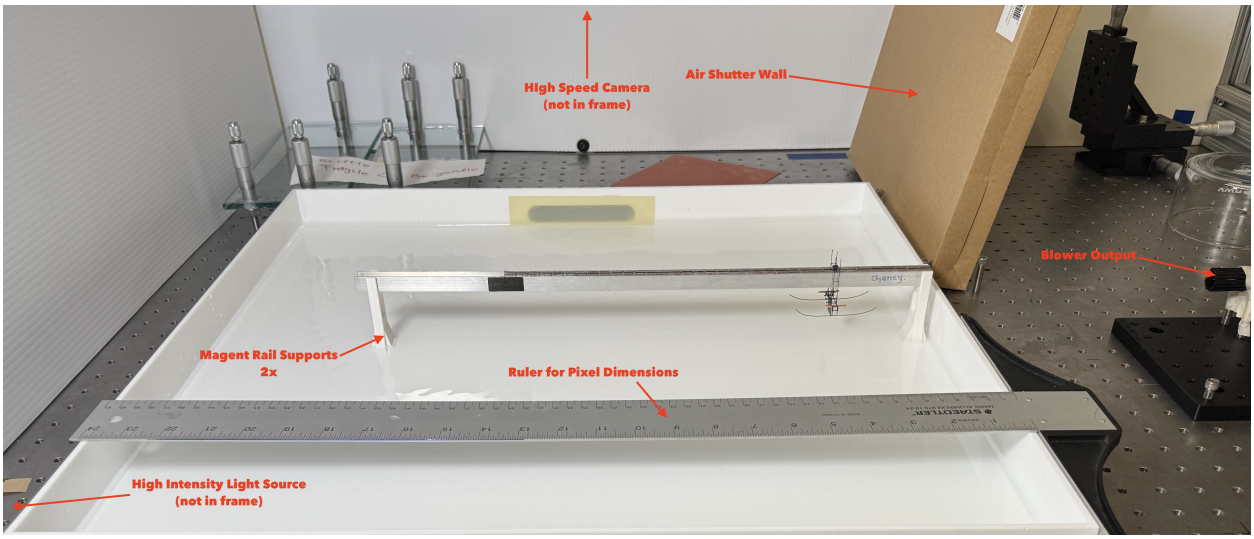

Figure 12: Experimental setup for Gammabot braking tests

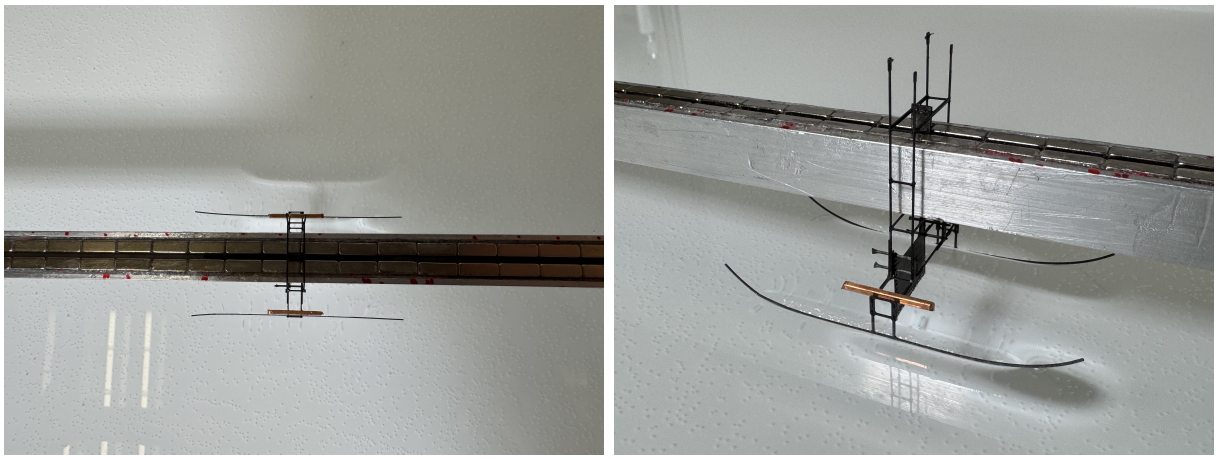

(a) Top view of magnetic rail (b) Side view of magnetic rail

Figure 13: Magnetic rail test configuration.

5.2 Data Collection and Iteration

We collected data at two brake depths (5 mm and 2 mm) and a no-brake baseline case. Because the water meniscus is approximately 2 mm to 3 mm deep, the actual wetted area was likely larger than the nominal immersion depth. We plan to complete additional experiments to accurately measure the brake depths; these trials were just to prove the effectivness of the brake and develop intuition for how K scales with brake depth. For each trial, the remained closed until the blower reached a steady speed to avoid the transient spin-up period. Once the flow was steady, the operator at the computer triggered the high-speed camera and the second operator quickly opened the shutter so the air jet could accelerate the robot; after the robot reached roughly mid-rail, the shutter was closed again, and recording continued until the robot came to rest or contacted the hard stops.

Four trials were recorded for each brake depth and for the no-brake case. Any run in which the robot broke surface tension at any point was discarded and repeated. The braking trials were then processed in MATLAB. Robot position was tracked in each frame of the high speed video. After the user selects a global crop region and a robot template, the script performs frame-by-frame normalized cross-correlation to localize the robot centroid, converts the tracked positions from pixels to meters, and computes displacement, velocity, and acceleration in time. These kinematic signals are smoothed using both Savitzky–Golay and Butterworth low-pass filters, and the resulting trajectories are visualized alongside their raw counterparts. The smoothed velocity and displacement are then used to fit an exponential decay model for $v(x)$ yielding the experimental lumped drag constant K_{exp}. Finally, the script exports a `decayResult` structure containing all relevant kinematic and fit data for

downstream plotting and analysis.

6 Results

Data for two trials at each depth are plotted in Figs. 14 to 16, with a common velocity and distance axis maintained within each depth. From the R^2 values reported in Table 1, the exponential velocity–distance model provides a strong representation of the decay behavior, both with and without the brake attached.

For both braked depths, the fitted decay constant K is smaller than the ideal value prescribed by the design calculations. This discrepancy is not necessarily problematic: the "ideal" K represents the value required to meet the 6 cm stopping criterion in a simplified model, whereas the experimentally fitted K captures the actual hydrodynamics, tank constraints, and unmodeled losses. What was more surprising is the limited variation in fitted K across the two brake depths. Because K is proportional to effective wetted area, one would expect a deeper brake to yield a larger K and thus a more rapid decay than a shallower brake.

The contrast between braked and unbraked behavior is much clearer. As shown in Fig. 17, the no-brake trials exhibit a much slower decay in velocity. Aggregating the fitted constants, the braked trials have a mean $K \approx 17.27$, whereas the no-brake trials have a mean $K \approx 3.16$, roughly one fifth of the braked value. This confirms that, even if depth-specific differences are small, the presence of the brake substantially increases the effective drag.

From Table 1 it is also evident that the starting velocities are fairly consistent within each condition. The initial velocity for the no-brake trials is approximately $2.5\times$ larger than that of the braked trials, yet the fitted K values within each group remain tightly clustered, indicating that the estimated decay constants are not strongly sensitive to modest changes in v_0 over the range tested.

Finally, the distance required to reach 5% of the initial velocity, $\Delta x_{5\%}$, shows a similar trend. Within the braked trials, $\Delta x_{5\%}$ is nearly constant across depths, contrary to the expectation that a deeper brake would achieve a shorter stopping distance from comparable initial speeds. However, when compared to the no-brake condition, the brake reduces the stopping distance to roughly one third of the unbraked value. In fact, the no-brake trials do not reach 5% of their initial velocity within the available magnetic rail length; the $\Delta x_{5\%}$ values reported for no-brake in Table 1 are extrapolated from the fitted exponential model rather than directly observed in the raw data.

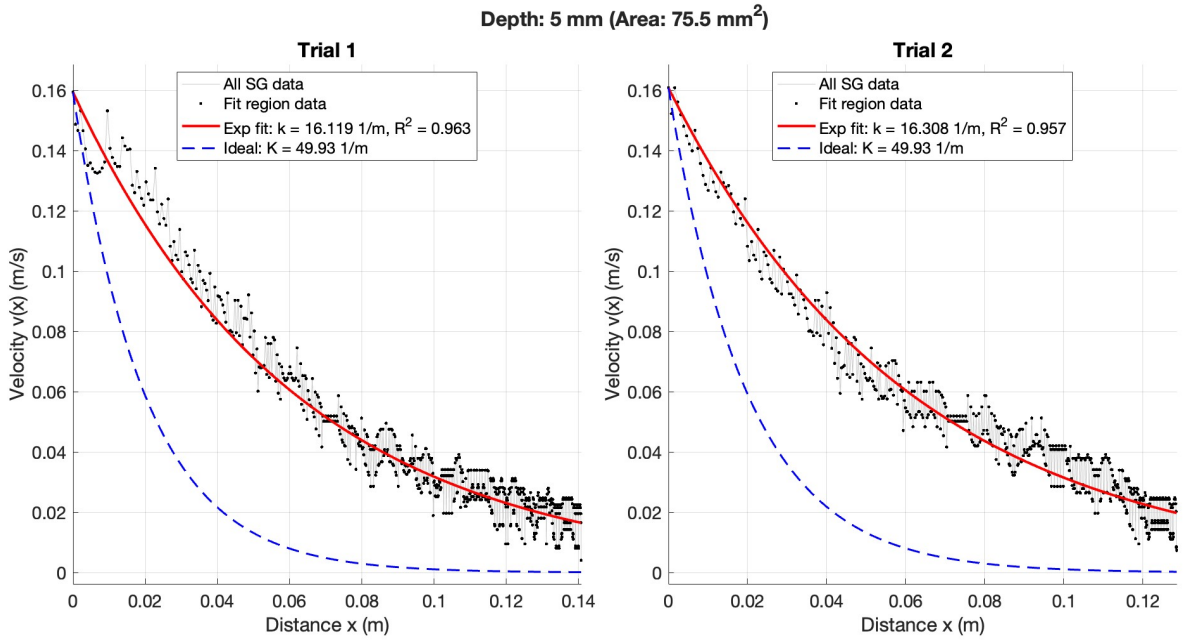

Figure 14: 5mm Brake Depth Data

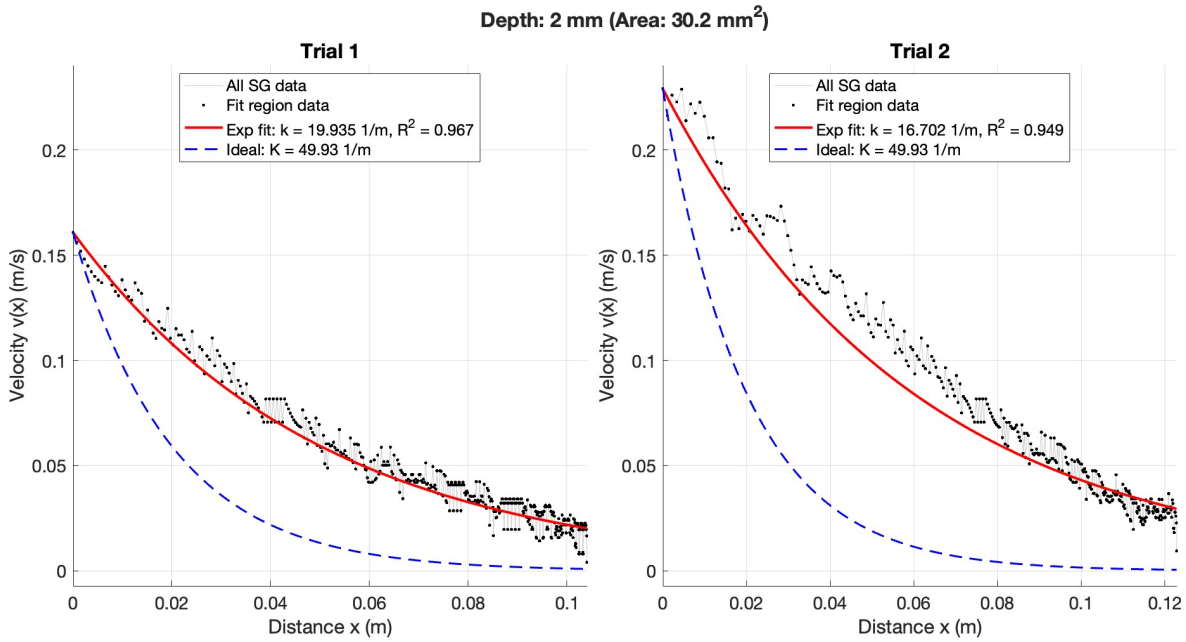

Figure 15: 2mm Brake Depth Data

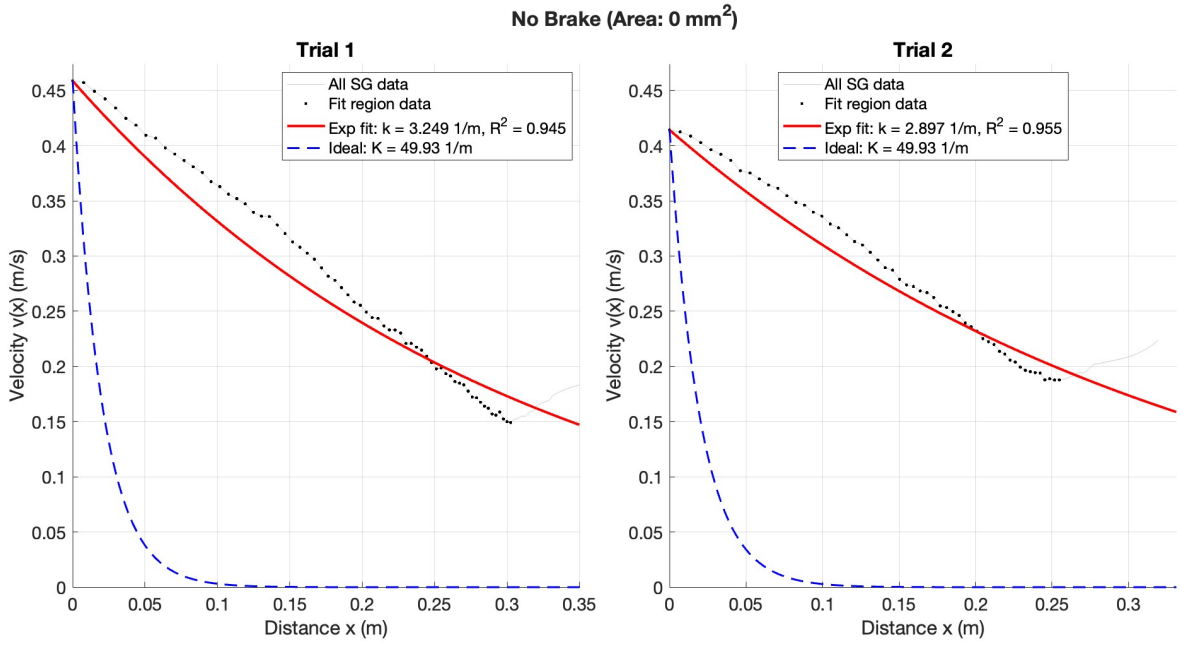

Figure 16: 0mm Brake Depth Data

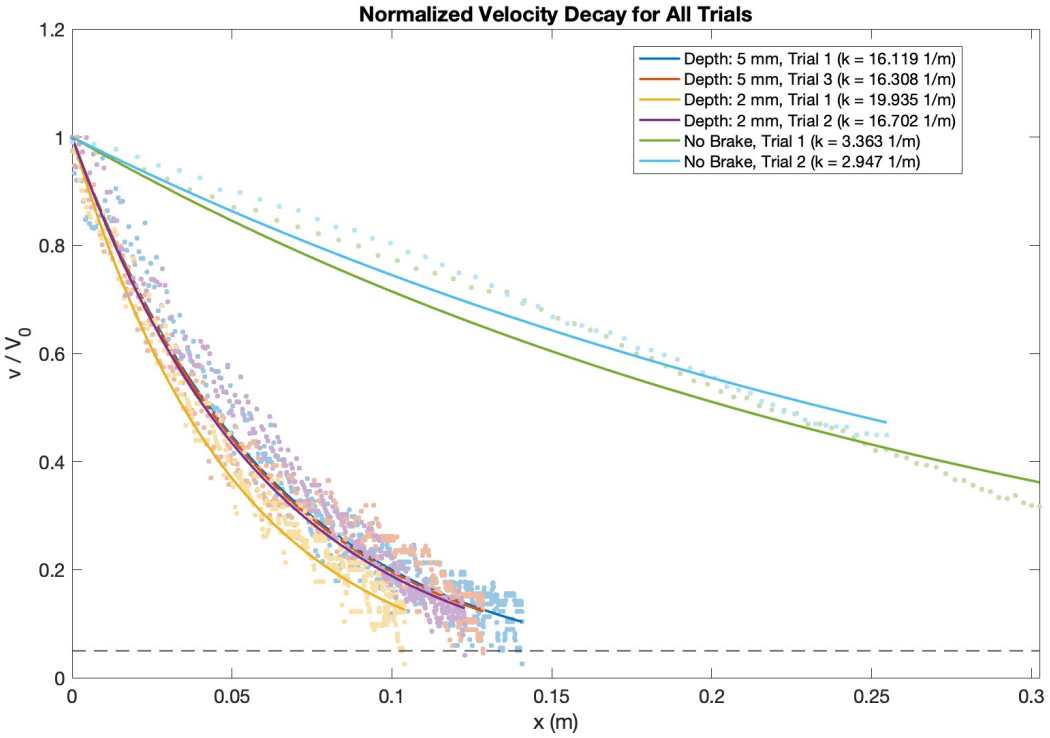

Figure 17: All trials with normalized velocity

Trial	V_{start} (m/s)	K(1/m)	$\Delta x_{5\%}$ (cm)	R^2
Depth 2 mm, Trial 1	0.1609	19.94	10.40	0.967
Depth 2 mm, Trial 2	0.2291	16.70	12.28	0.949
Depth 5 mm, Trial 1	0.1595	16.12	14.07	0.963
Depth 5 mm, Trial 2	0.1609	16.31	12.85	0.957
No Brake, Trial 1	0.4587	3.25	30.25	0.945
No Brake, Trial 2	0.4142	2.90	25.47	0.955

Table 1: Summary of exponential decay fits for each trial, showing starting velocity, fitted decay constant k, distance to reach 5% of the starting velocity, and coefficient of determination R^2.

7 Discussion

In an ideal experiment, the difference between the design decay constant K_{ideal} and the experimentally fitted K_{exp} would be the primary quantity of interest. The broader goal is to construct an empirical relationship $A(K_{\text{exp}})$ (or a lookup table) so that, given a target decay constant K_{target} derived from a desired initial velocity and stopping distance, one can determine the required brake area. For a sufficiently dense set of experimental trials, the area associated with the K_{exp} value closest to K_{target} would then be selected as the geometry expected to meet the performance specification.

A key reason the fitted K values for the two brake depths appear so similar is that in the conducted trials, the robot only reached an average initial speed of $\bar{v}_0 \approx 0.178\,\text{m/s}$ with the brake engaged, far below the design value of $0.7\,\text{m/s}$. Because the quadratic drag force scales as $F_D \propto v^2$, the absolute braking forces at these lower speeds are relatively small. Consequently, unmodeled effects (including friction in the magnet rail, slight tank mis-leveling that changes the effective immersion along the track, and wave disturbances generated by the blower) constitute a much larger fraction of the total force than they would at higher speeds (assuming these unmodeled effects do not also scale with v^2). Under these conditions, variations due to brake depth are partially diluted, so the fitted K values for different depths cluster more tightly than expected.

To obtain more discriminating measurements, the experiment must either use a substantially longer water tank, allowing the robot to accelerate to near design speed with the brake already immersed, or adopt a actuated design in which the robot accelerates with the brake out of the water and the brake is rapidly deployed once the desired speed is reached. The latter approach would enable initial velocities closer to the $0.4\,\text{m/s}$ values observed in the

no-brake trials while still isolating the braking dynamics.

Finally, frequency-domain analysis of the velocity data revealed significant high-frequency displacment noise in the FFT, consistent with slight frame-to-frame movement in the tracking results. This suggests that increasing the robot velocity would require an increase in frame rate to reduce measurement noise in the extracted $x(t)$ and $v(x)$ profiles.

8 Conclusions and Next Steps

This work has created valuable infrastructure for future centimeter-scale experiments, including both the physical prototype and a tested experimental workflow. The data highlights a significant success of the overall Gammabot braking prototype: there is a clear reduction in stopping distance whenever the brake is deployed compared to the no-brake case. As my first extended project at the insect scale and on water-skimming robots, this work has clarified the key factors that govern design, fabrication, and testing for such systems and better equipped me to carry out the next step of Gammabot braking experiments.

The results show that a more accurate experiment is needed to either reveal clearer variation among depths or, at minimum, increase confidence in the data so trends can be interpreted physically rather than attributed to experimental limitations. Next-step experiments should prioritize achieving higher top speeds and improving the magnetic rail setup. The largest limitation in the current campaign is likely the unmodeled blower used to accelerate the robot, which should be replaced either by the Gammabot's own powered wings or by a more controlled mechanism such as a pulley–weight system that can provide a known and repeatable acceleration. With a cleaner input forcing, future work can focus on establishing an empirical relationship (or at least a consistent trend) between the ideal and experimental values of the lumped parameter K. Once the dependence of K on brake depth is better characterized, subsequent tests can more fully exploit the eight discrete immersion settings available on the brake plate.

9 Acknowledgments

I would like to extend a special thank you to Prof. Farrell Helbling for this opportunity and research guidance throughout the semester. Massive thank you to Cheney Zhang for extensive experimental and fabrication support; to Harry Gao for general Gammabot guidance, MATLAB help, and design feedback; to Cameron Urban for assistance with modeling and physics explanations; Prof. Brian Kirby for advising on initial fluid-dynamics approximations that informed experimental design direction; and to Jack Long for feedback on

experimental procedures and help with data collection and photography.

References

[1] A. M. Jones, "Drag Coefficients for Flat Plates, Spheres, and Cylinders Moving at Low Reynolds Numbers in a Viscous Fluid," Master's thesis, Oregon State College, Corvallis, OR, 1958. Available at `https://scispace.com/pdf/drag-coefficients-for-flat-plates-spheres-and-cylinders-1b4c6sr09j.pdf`.

[2] H. Gao, S. Jung, and E. F. Helbling, "High-speed interfacial flight of an insect-scale robot," in *2024 IEEE International Conference on Robotics and Automation (ICRA)*, Yokohama, Japan, May 2024, pp. 6006–6013. Available at `https://ieeexplore.ieee.org/document/10611592`.

[3] M. Deserno, "The shape of a straight fluid meniscus," lecture notes, Max-Planck-Institut für Polymerforschung, Mainz, Germany, Mar. 2004. Available at `https://www.cmu.edu/biolphys/deserno/pdf/meniscus.pdf`.

[4] D. F. Elger, B. A. LeBret, C. T. Crowe, and J. A. Roberson, *Engineering Fluid Mechanics*, 12th ed. Hoboken, NJ, USA: Wiley, 2019.

[5] Toray Advanced Composites, *Toray RS-3 Toughened Cyanate Ester Resin Product Data Sheet*, rev. 2.0, Jul. 2019. Available: Toray Advanced Composites.